Chapter 6

Conclusions

6.1 Summary

Theoretical arguments presented in Chapter 2 show that when $\beta = 0$ a slight generalisation to the standard barotropic quasigeostrophic vorticity equation makes it applicable to linear and moderately nonlinear flow in a basin with $O(1)$ depth variations. Although β is equivalent to the depth gradient in terms of the ambient potential vorticity gradient in the quasigeostrophic limit of small depth variations, β has a direct effect on the horizontal divergence of the linear flow outside the Ekman layers, whereas the depth gradient is "felt" by this flow only through the vertical stretching, which is very restricted when $\beta = 0$ as a consequence of the Taylor-Proudman theorem. The horizontal divergence is therefore very small in the linear limit, so to a good approximation the vorticity equation governing the low-Rossby number horizontal flow is identical to the standard quasigeostrophic vorticity equation except for the inclusion of the actual depth variation in the denominator of the stretching term. This generalised formulation retains the simplicity and conservation properties of the standard barotropic quasigeostrophic vorticity equation.

This generalised formulation was implemented in a numerical model based on a code developed by Page (1982) and Becker & Page (1990). A novel implementation allowed the orographic term to be evaluated more accurately in regions where the bottom slope changes abruptly. The accuracy of the formulation and its implementation were tested in Chapters 3 and 4 by a detailed comparison with laboratory results, using both the sliced cylinder and sliced cone models and a wide range of the governing parameters. The numerical results closely matched those found in the laboratory in terms of the flow structure and its dependence on the governing parameters in both models. There was also good agreement in the critical Rossby number at which the flow became unstable, and the numerical model convincingly reproduced the observed physical structure of the instabilities. The main area of disagreement was in the onset of aperiodic eddy shedding in the sliced cylinder, but this occurred under strongly nonlinear conditions for which the formulation becomes inaccurate. There were also minor differences related to the absence of a Stewartson $E^{\frac{1}{3}}$ sidewall layer in the numerical model of the sliced cylinder.

Analysis of the numerical results in Chapters 3, 4 and 5 has also revealed many details of the dynamics of these models which could not be determined in the laboratory. The numerical results provided an opportunity to test the linear theory of Griffiths & Veronis (1998). The predicted vorticity balances agreed with those found in the numerical results in the interior and on most of the upper slope, but were significantly different on the slope at the west and in the shear layer near the bottom of the sloping sidewall. These differences were shown to be due to shortcomings in the analytical approach used by Griffiths and

Veronis. The numerical results also showed that potential vorticity dissipation in the sliced cone is distributed around the bottom of the slope, rather than being localised at the east as suggested by Griffiths & Veronis (1997, 1998). The linear circulation pattern was explained using the thermal analogy of Welander (1968), which shows that the distributed potential vorticity dissipation is due to the closure of geostrophic contours in this geometry.

The numerical results have also provided insights into the dynamics of the flow under nonlinear conditions. The numerical model showed that in the sliced cylinder under the no-slip boundary condition the viscous sublayer of the western boundary current must separate from the boundary at large Rossby number to enable the outflow to change its potential vorticity to match that in the interior. Thus separation is a response to a “crisis” due to excessive potential vorticity dissipation in the sublayer, rather than insufficient dissipation in the outer western boundary current as suggested by Holland & Lin (1975) and Pedlosky (1987*b*). This view of the separation process also explains why separation does not occur under the free-slip boundary condition. The role of this potential vorticity “crisis” in the separation process is made particularly clear in this model, since the basin has no corners and the model lacks stratification, bottom topography and spatial variation in the wind stress.

The numerical results allowed the stability boundaries in both models to be refined. It was shown that there is a regime in the sliced cylinder in which the vortex sheets of the western boundary current separate from the boundary, but there is no reversed flow. The secondary role of stagnation points in the separation process is consistent with the potential vorticity crisis mechanism.

The numerical results also clarified the way in which the western boundary current instability in the sliced cone disappears at large Rossby and/or Ekman number, and demonstrated that instability arises in both models as a result of supercritical Hopf bifurcations. A study was also conducted to determine the location of the stability boundary as a function of the aspect ratio of the sliced cylinder, which demonstrated that the flow is stabilised in narrow basins such as those used by Beardsley (1969, 1972, 1973) and Becker & Page (1990).

Instability in the sliced cone is found only under anticyclonic forcing. This remarkable dependence of the stability on the sign of the wind forcing is shown to be due to the combined effects of the relative vorticity and topography in determining the shape of the potential vorticity contours. The vorticity at the bottom of the sidewall smooths out the potential vorticity contours under cyclonic forcing, but distorts them into highly contorted shapes under anticyclonic forcing. These changes are also related to the flow direction relative to the direction of Rossby wave phase propagation, which determines that flows dominated by inertial boundary layers are found only under cyclonic forcing, whilst the anticyclonically forced flow will be dominated by standing Rossby waves. The complex structure and small scales of the flow under anticyclonic forcing make it prone to barotropic instability under strong forcing. In contrast, under cyclonic forcing the scales of motion become larger as the Rossby number is increased (since the inertial boundary layers grow to fill the basin) and the flow remains stable even under very strong forcing. The alterations to the potential vorticity structure under cyclonic forcing reduce the potential vorticity changes experienced by fluid columns, and the flow approaches a free inertial circulation under very strong forcing. In contrast, the potential vorticity changes remain large under strong anticyclonic forcing.

The numerical results have shown that the two types of instability found in the sliced cone under anticyclonic forcing are closely related to the western boundary current instability and “interior instability” identified by Meacham & Berloff (1997*b*). The western boundary current instability was similar to that seen by Bryan (1963) and Kamenkovich *et al.* (1995) and consisted of a train of growing waves at the western side of the interior. It was shown that these perturbations were trapped in this region at small amplitude because their northward phase speed exceeds that of the fastest interior Rossby wave with the same meridional wavenumber, as discussed by Ierley & Young (1991). In contrast the "jet" (or "interior") instability induced much more widely distributed variability, consistent with the numerical results of Meacham & Berloff (1997*b*). The jet instability was also found in the sliced cylinder, but the western boundary current instability was not. This suggests that the sloping sidewall destabilises the western boundary current in the sliced cone under anticyclonic forcing.

A study was also undertaken of the sensitivity of the horizontal flow in these models to the choice of boundary conditions at the "coast". The flow in the sliced cylinder was dramatically different when the no-slip boundary condition was replaced by the free-slip condition: the western boundary current overshot the northernmost point and entered the interior from the east, and the flow was stable even under very strong forcing. There was no separated jet, because the viscous sublayer is absent with this boundary condition. This behaviour is analogous to that found by Veronis (1966*b*) and Blandford (1971) under free-slip conditions. In contrast, the flow in the sliced cone was completely insensitive to the choice of boundary condition (even with an approximate super-slip condition), except in the immediate vicinity of the "coast". This insensitivity results from the extremely strong topographic steering near the edge of the basin due to the vanishing depth, which demands a balance between wind forcing and Ekman pumping on the upper slope, regardless of the "coastal" boundary condition. The continental slope also isolates the Sverdrup return flow from the "coast", so the potential vorticity supplied by the wind is dissipated in an internal shear layer. This insensitivity to the choice of boundary condition extends the linear result of Kubokawa & McWilliams (1996) into the nonlinear regime.

6.2 Applications

It has been demonstrated that a slightly modified quasigeostrophic formulation can be used to accurately model moderately nonlinear barotropic flow on an f-plane with $O(1)$ depth variations. The simplicity and numerical efficiency of this formulation may make it advantageous to use in other numerical or analytical studies of laboratory or oceanic flows.

Although many of the detailed features of the sliced cylinder and sliced cone circulations are probably specific to these models, some of the results obtained may be indicative of more general properties of rotating flow. The stability and "inertial runaway" observed in cyclonic flow in the sliced cone are likely to be general features of pseudo-westward *barotropic* circulation in a geostrophically guided domain, since the alignment of streamlines and potential vorticity contours via internal inertial boundary layers does not depend on details of the topography. The sliced cone results also suggest (as does the linear theory of Kubokawa & McWilliams, 1996) that the inclusion of sloping boundaries in numerical ocean models may reduce the sensitivity of the circulation to the poorly-known lateral boundary condition by allowing the Sverdrup circulation to close without encountering the lateral boundary.

One must be cautious in drawing conclusions about ocean circulation from this highly idealised modelling work, since it neglects several features (such as stratification) which are known to play an important dynamical role. However the barotropic component of the circulation in the oceans may include contributions from the processes identified in this study.

The smoothly curving boundary and spatially uniform wind stress curl in the sliced cylinder allow the potential vorticity "crisis" in the sublayer and its association with western boundary current separation to be clearly revealed. This separation process requires only lateral viscosity, vorticity advection and an ambient potential vorticity gradient and is therefore likely to be relevant to separation of western boundary currents in other barotropic models, such as that studied by Moro (1988). It is possible that a similar process plays a role in western boundary current separation in the oceans, although the dynamics are likely to be much more complex due to isopycnal outcropping, spatially variable forcing and complex topography.

The sliced cone results show that the closure of geostrophic contours has a profound effect on the circulation, leading to a strong topographically steered current over the sloping sidewall. This recirculation is absent in a geostrophically blocked domain such as a midlatitude ocean basin, in which the depth does not go to zero at the northern and southern boundaries. The model is therefore more relevant to barotropic wind-driven circulation in an enclosed sea which is large enough for the Coriolis effect to be dynamically significant. A superficially likely candidate is the Black Sea, which has bottom topography that roughly resembles that in the sliced cone (although the slope of the sidewalls is not nearly so uniform). The flow in this basin is dominated by a strong, persistent cyclonic recirculation (the Rim Current) which is confined over the steepest topographic slope (Oguz *et al.*, 1994). The topographic steering of this circulation is analogous to that seen over the slope in the sliced cone. A naïve application of the sliced cone results suggests that the large-scale structure of this cyclonic circulation would be stable under steady forcing. However numerical modelling shows that this is not the case (Oguz & Malanotte-Rizzoli, 1996): even under steady forcing the Rim Current exhibits propagating meanders which evolve to shed mesoscale eddies. This behaviour is due to baroclinic instability (Oguz *et al.*, 1994), which arises because the Rim Current is also a frontal boundary.

The destabilising effect of the continental slope revealed in the sliced cone experiments may be relevant to western boundary currents in the ocean, but it is likely that baroclinic energy conversion would also play an important role in enhancing the instability (Berloff & McWilliams, 1999*b*; Berloff & Meacham, 1998).

6.3 Directions for future work

The results presented here open up several avenues for further research.

The numerical results demonstrate that separation of the western boundary current occurs in response to a potential vorticity "crisis" in the viscous sublayer. This insight could possibly be elaborated into a more deductive theory of western boundary current separation which would predict the separation position and the critical Rossby number. An investigation of the role of the higher-order pressure gradient (Baines & Hughes, 1996; Haidvogel *et al.*, 1992) in the momentum balance in the separation region would also be informative.

Of particular interest would be an analysis (along the lines taken by Ierley & Young, 1991) of the mechanism by which the sloping sidewall destabilises the western boundary current in the sliced cone. Further insight into the nature of the instabilities and their role in the transition to chaos under strong forcing would be gained by applying the methods of dynamical systems theory in the manner of Dijkstra & Katsman (1997); Jiang *et al.* (1995); Meacham & Berloff (1997*a*); Sheremet *et al.* (1997) and others[1].

[1] A preliminary investigation of this type has been conducted (Kiss, 1999) but the results have not been

Further numerical and laboratory work could also be conducted using different bottom topography, to investigate the effects of a western sidewall in a basin which is geostrophically blocked rather than guided. The manner in which the flow approaches that in the sliced cylinder as the sidewall becomes steeper would also be informative, and could be related to the theoretical work of Kubokawa & McWilliams (1996). Of particular interest is the degree to which the numerical results remain independent of the lateral boundary condition when the topography allows the internal shear layer to approach the boundary.

included here because they were affected by numerical problems due to a non-conservative formulation used in a previous version of the code.

Appendix A

The Ekman layer on a slope

Pedlosky (1987a, section 4.9) derives an expression for Ekman pumping on a slope for the oceanographically relevant case of differing vertical and horizontal eddy diffusivities. A simpler derivation is presented here for the special case of isotropic viscosity (as in the laboratory models).

Consider a flow over a rigid lower boundary with uniform slope $s = \tan\alpha$, where α is the bottom slope angle to the horizontal (see figure A.1). We choose two sets of right-handed Cartesian coordinates, (x, y, z) and (x', y', z'), where x is the horizontal coordinate in the direction of increasing height of the topography[1] and z is vertical (aligned with the planetary rotation axis), whilst x' is tangent to the boundary and z' normal to the boundary and directed into the fluid. The coordinate axes y and y' (directed into the page in figure A.1) are identical. The velocity $\mathbf{u}$ has components (u, v, w) and $(u', v' = v, w')$ relative to these coordinates.

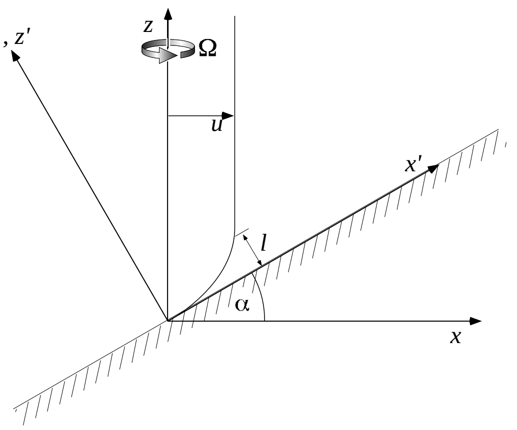

Figure A.1: Definition sketch for Ekman pumping on a slope.

The component of the steady, linear vorticity equation (2.6) in the direction of the z' axis is

$$\frac{\partial w'}{\partial z} = \cos\alpha \frac{\partial w'}{\partial z'} + \sin\alpha \frac{\partial w'}{\partial x'} = -\frac{E}{2}\nabla^2\zeta', \tag{A.1}$$

where $\zeta' = \hat{\mathbf{k}}' \cdot \nabla \times \mathbf{u}$ is the component of the vorticity normal to the boundary and $\hat{\mathbf{k}}'$ is the unit vector in the direction of increasing z'. We now make the boundary-layer approx-

[1]The definitions of x and y in this appendix differ from those used throughout the rest of this thesis, where the x axis points eastwards, as in figure 2.1.

imation: we assume that close to the boundary $\frac{\partial}{\partial z'} \gg \frac{\partial}{\partial x'}, \frac{\partial}{\partial y'}$ by defining the stretched coordinate $\eta = z'/l$, where $l \ll 1$ is the boundary layer thickness (to be determined shortly), such that $\frac{\partial}{\partial \eta}$ is of the same magnitude as $\frac{\partial}{\partial x'}$ and $\frac{\partial}{\partial y'}$. Using this scaling and assuming $s \ll l^{-1}$ (i.e. the bottom slope is not too steep), the dominant terms in (A.1) yield

$$\cos\alpha \left(\frac{\partial u'}{\partial x'} + \frac{\partial v'}{\partial y'} \right) = l^{-2} \frac{E}{2} \frac{\partial^2 \zeta'}{\partial \eta^2} \tag{A.2}$$

(the continuity equation (2.2) was used so that both sides involve only u' and v'). In order to have both sides the same magnitude we choose $l = \sqrt{\frac{E}{\cos\alpha}} = \sigma E^{\frac{1}{2}}$, where $\sigma = \sqrt[4]{1+s^2}$, to obtain

$$2 \left(\frac{\partial u'}{\partial x'} + \frac{\partial v'}{\partial y'} \right) = \frac{\partial^2 \zeta'}{\partial \eta^2}. \tag{A.3}$$

This vorticity equation indicates that, as for a horizontal bottom boundary, the Ekman layer balance is between the generation of relative vorticity by stretching of the normal component of the planetary vorticity in the direction normal to the boundary, and viscous diffusion of this vorticity in the same direction. The Ekman layer is thicker on a slope (by a factor of σ) because the component of the planetary vorticity normal to the boundary is reduced, so stretching in this direction is less effective in generating relative vorticity and a weaker vorticity gradient is therefore sufficient to dissipate it.

Having determined the boundary layer thickness, we will now determine the flow in the Ekman layer in order to find the Ekman pumping velocity w. Using the boundary-layer approximation with the boundary layer thickness $l \ll 1$, the dominant terms of the x', y' and η components of the steady, linear momentum equation yield

$$v' = \frac{\sigma^2}{2} \frac{\partial p}{\partial x'} - \frac{1}{2} \frac{\partial^2 u'}{\partial \eta^2} \tag{A.4}$$

$$u' = -\frac{\sigma^2}{2} \frac{\partial p}{\partial y'} + \frac{1}{2} \frac{\partial^2 v'}{\partial \eta^2} \tag{A.5}$$

$$0 = \frac{\partial p}{\partial \eta}, \tag{A.6}$$

respectively. By combining these we obtain the equations

$$v' + \frac{1}{4} \frac{\partial^4 v'}{\partial \eta^4} = \frac{\sigma^2}{2} \frac{\partial p}{\partial x'} \tag{A.7}$$

$$u' + \frac{1}{4} \frac{\partial^4 u'}{\partial \eta^4} = -\frac{\sigma^2}{2} \frac{\partial p}{\partial y'}, \tag{A.8}$$

and note that since $\frac{\partial p}{\partial \eta} = 0$, $\frac{\partial p}{\partial x'}$ and $\frac{\partial p}{\partial y'}$ have the same values as outside the Ekman layer.

The general solutions to (A.7) and (A.8) which satisfy (A.4) and (A.5) and remain finite for $\eta \to \infty$ are

$$v' = \frac{\sigma^2}{2} \frac{\partial p}{\partial x'} + e^{-\eta} \left\{ C_1 \cos\eta + C_2 \sin\eta \right\} \tag{A.9}$$

$$u' = -\frac{\sigma^2}{2} \frac{\partial p}{\partial y'} + e^{-\eta} \left\{ C_1 \sin\eta - C_2 \cos\eta \right\}, \tag{A.10}$$

which represent the familiar Ekman spiral. The coefficients C_1 and C_2 are independent of η; applying the no-slip boundary condition $u' = v' = 0$ at $\eta = 0$ gives $C_1 = -\frac{\sigma^2}{2}\frac{\partial p}{\partial x'}$ and $C_2 = -\frac{\sigma^2}{2}\frac{\partial p}{\partial y'}$. Using these values we find

$$v' = \frac{\sigma^2}{2}\left\{\left[1 - e^{-\eta}\cos\eta\right]\frac{\partial p}{\partial x'} - e^{-\eta}\sin\eta\frac{\partial p}{\partial y'}\right\} \tag{A.11}$$

$$u' = \frac{\sigma^2}{2}\left\{-e^{-\eta}\sin\eta\frac{\partial p}{\partial x'} - \left[1 - e^{-\eta}\cos\eta\right]\frac{\partial p}{\partial y'}\right\}. \tag{A.12}$$

Using these expressions we can find the velocity w' normal to the boundary in the limit $\eta \to \infty$, by applying the continuity equation $\frac{\partial u'}{\partial x'} + \frac{\partial v'}{\partial y'} + \sigma^{-1}E^{-\frac{1}{2}}\frac{\partial w'}{\partial \eta} = 0$ to the Ekman layer as a whole, given the boundary condition $w = 0$ at $\eta = 0$:

$$\begin{aligned} w'(\eta \to \infty) &= \int_0^\infty \frac{\partial w'}{\partial \eta}\,\mathrm{d}\eta \\ &= -\sigma E^{\frac{1}{2}}\int_0^\infty \frac{\partial u'}{\partial x'} + \frac{\partial v'}{\partial y'}\,\mathrm{d}\eta \\ &= \frac{\sigma^3}{2}E^{\frac{1}{2}}\int_0^\infty \left(\frac{\partial^2 p}{\partial x'^2} + \frac{\partial^2 p}{\partial y'^2}\right) e^{-\eta}\sin\eta\,\mathrm{d}\eta \\ &= \frac{\sigma^3}{4}E^{\frac{1}{2}}\left(\frac{\partial^2 p}{\partial x'^2} + \frac{\partial^2 p}{\partial y'^2}\right). \end{aligned} \tag{A.13}$$

We now need to use this result to obtain the vertical velocity w_B at the top of the Ekman layer. Since $w' = w\cos\alpha - u\sin\alpha$ we have

$$\begin{aligned} w_B &= \frac{w'(\eta \to \infty)}{\cos\alpha} + su \\ &= \frac{\sigma^3}{4\cos\alpha}E^{\frac{1}{2}}\left(\frac{\partial^2 p}{\partial x'^2} + \frac{\partial^2 p}{\partial y'^2}\right) + su, \end{aligned} \tag{A.14}$$

where u is the x-velocity in the bulk of the fluid (outside the Ekman layer). Now $\frac{\partial^2 p}{\partial y'^2} = \frac{\partial^2 p}{\partial y^2}$ and $\frac{\partial^2 p}{\partial x'^2} = \cos^2\alpha\frac{\partial^2 p}{\partial x^2}$ (since $\frac{\partial p}{\partial \eta} = 0$), so this expression becomes

$$\begin{aligned} w_B &= \frac{\sigma^3}{4}E^{\frac{1}{2}}\left(\cos\alpha\frac{\partial^2 p}{\partial x^2} + \frac{1}{\cos\alpha}\frac{\partial^2 p}{\partial y^2}\right) + su \\ &= \frac{\sigma}{4}E^{\frac{1}{2}}\left(\frac{\partial^2 p}{\partial x^2} + (1+s^2)\frac{\partial^2 p}{\partial y^2}\right) + su, \end{aligned} \tag{A.15}$$

where in the second line we have used $\sigma^2 = 1/\cos\alpha$ and $1/\cos^2\alpha = 1 + s^2$. If we equate p with the geostrophic pressure 2ψ of the interior flow, we obtain

$$w_B = \frac{\sigma}{2}E^{\frac{1}{2}}\left(\zeta - s^2\frac{\partial u_\psi}{\partial y}\right) + su, \tag{A.16}$$

where $\zeta = \nabla_H^2\psi$ is the vertical component of the vorticity in the bulk of the fluid, and $u_\psi = -\frac{\partial \psi}{\partial y}$ is also in the bulk of the fluid. All that remains is to write this expression in a form which is independent of the choice of horizontal axes. Since x and y are defined in terms of the topography, we can replace su with $\mathbf{u}_H \cdot \nabla_H h$ and u_ψ with $\mathbf{u}_\psi \cdot \hat{\mathbf{s}}$ (where

$\mathbf{u}_\psi = \hat{\mathbf{k}} \times \nabla_H \psi$, $\hat{\mathbf{s}} = s^{-1} \nabla_H h$ and h is the height of the bottom), and also replace $\frac{\partial}{\partial y}$ with $-\left(\hat{\mathbf{s}} \times \hat{\mathbf{k}}\right) \cdot \nabla_H$. This yields equation (2.16):

$$w_B = \mathbf{u}_H \cdot \nabla_H h + \frac{\sigma}{2} E^{\frac{1}{2}} \left\{ \zeta + s^2 \left(\hat{\mathbf{s}} \times \hat{\mathbf{k}}\right) \cdot \nabla_H (\mathbf{u}_\psi \cdot \hat{\mathbf{s}}) \right\}. \tag{A.17}$$

Although the analysis leading to this expression was derived for a uniform slope, the coordinate-free form can be also be used when $\nabla_H h$ varies with position, provided this variation is small on the scale of the Ekman layer thickness $l = \sigma E^{\frac{1}{2}}$.

Appendix B

Details of the numerical implementation

The numerical code is based on that supplied by Michael Page (Monash University) and described in detail in his doctoral thesis (Page, 1981). The general algorithmic structure of Page's vorticity solver was retained in this work, but many changes were made to its details (summarised in section 2.4) so this appendix presents a detailed discussion of this aspect of the code. Page's Poisson solver was retained without modification, apart from efficiency improvements; details on the Poisson solver can be found in Page (1981). An overview of the complete code is presented in figure 2.2 on page 28.

B.1 Scaling in Page's code

The scaling chosen by Page for his code is different from that used in this thesis, in that he scaled the length, time and velocity by a, $\tau|\Omega|^{-1}$ and $|\epsilon\Omega|a$, respectively (rather than H_o, $|\epsilon\Omega|^{-1}$ and $|\epsilon\Omega|H_o)$, where $\tau = 2^{-1}E^{-\frac{1}{2}}$. The temporal scaling is in terms of the spin-up timescale due to Ekman pumping rather than the advective timescale, allowing the unsteady, linear adjustment to be studied. With this scaling, the vorticity equation (2.33) becomes

$$\frac{\partial \zeta_p}{\partial t_p} + \tau Ro \nabla_{Hp} \cdot \left(\mathbf{u}_{\psi p}\zeta_p\right) = 2\tau\left(\frac{\partial w}{\partial z}\right)_p + \tau E_p \nabla^2_{Hp}\zeta_p, \tag{B.1}$$

where

$$\left(\frac{\partial w}{\partial z}\right)_p = \nabla_{Hp}\cdot\left(\mathbf{u}_{\psi p}\ln D_p\right) + \frac{E_p^{\frac{1}{2}}}{2D_p}\left[\zeta_{Tp} - (1+\sigma)\zeta_p - \sigma s^2\left(\hat{\mathbf{s}}\times\hat{\mathbf{k}}\right)\cdot\nabla_{Hp}(\mathbf{u}_{\psi p}\cdot\hat{\mathbf{s}})\right], \tag{B.2}$$

$E_p = \Lambda^{-2}E$, $\zeta_p = \zeta$, $\mathbf{u}_{\psi p} = \Lambda^{-1}\mathbf{u}_{\psi}$, $\psi_p = \Lambda^{-2}\psi$ and the subscript p distinguishes quantities with Page's scaling. This scaling was retained in my version of the code, but for clarity I will continue to use the same scaling as in the rest of this thesis in the following exposition.

B.2 Spatial discretisation

Using polar coordinates we write $\mathbf{u}_{\psi} = u\hat{\mathbf{r}} + v\hat{\theta}$, where $\hat{\mathbf{r}}$ and $\hat{\theta}$ are the radial and azimuthal unit vectors (throughout this appendix u and v denote the radial and azimuthal components $-\frac{1}{r}\frac{\partial\psi}{\partial\theta}$ and $\frac{\partial\psi}{\partial r}$ of the horizontally nondivergent velocity, rather than the eastward and northward velocity components as in the rest of this thesis). Using a polar grid with uniform radial and azimuthal spacing Δ_r and Δ_θ we denote the radius and azimuth at grid indices (i,j) by $r_i = i\Delta_r$ and $\theta_j = (j-1)\Delta_\theta$ respectively. The indices are taken to lie in the ranges $0 < i < N_i$, $1 < j < N_j$; note that the j indices are cyclic, so $j = N_j + 1$ is identified with $j = 1$, et cetera. The velocity at (i,j) is denoted by $(u_{i,j}, v_{i,j}) \equiv (u(r_i,\theta_j), v(r_i,\theta_j))$. It is advantageous to use the quantity $U \equiv ru = -\frac{\partial\psi}{\partial\theta}$ instead of u since this allows us to define $U = 0$ at the origin, and avoid the singularity in u.

We will now write down the terms in the vorticity equation (2.33) as they appear under spatial discretisation on this polar grid[1]. We will utilise Gauss' theorem to write the terms which appear as divergences (the advection, orographic stretching and lateral viscosity) in terms of the flux through the boundary of a cell enclosing the point in question. Using the same fluxes at the boundaries of adjacent cells ensures conservation of vorticity, so that the numerical method retains the integral property (2.42).

Averaging the advective term over the region $r_{i-1} \le r \le r_{i+1}$, $\theta_{j-1} \le \theta \le \theta_{j+1}$ (and considering the values of the velocity and vorticity at the midpoints of the sides to be representative of their values across the width of each side) we obtain

$$\begin{aligned}\left[\nabla_H \cdot \left(\mathbf{u}_\psi \zeta\right)\right]_{i,j} = 2A_{i,j}^{-1}[\quad & \Delta_\theta \left(U_{i+1,j}\zeta_{i+1,j} - U_{i-1,j}\zeta_{i-1,j}\right) \\ & +\Delta_r \left(v_{i,j+1}\zeta_{i,j+1} - v_{i,j-1}\zeta_{i,j-1}\right)]\end{aligned} \tag{B.3}$$

where $A_{i,j} = 4r_i\Delta_r\Delta_\theta$ is the area of this region, and we have used second-order differences to obtain

$$U_{i,j} = -\left(\frac{\psi_{i,j+1} - \psi_{i,j-1}}{2\Delta_\theta}\right) \tag{B.4}$$

and

$$v_{i,j} = \frac{\psi_{i+1,j} - \psi_{i-1,j}}{2\Delta_r}. \tag{B.5}$$

The differencing scheme (B.3) is equivalent to the Jacobian $-\mathbb{J}_{i,j}^{+\times}(\zeta,\psi)$ in Arakawa's notation (Arakawa, 1966), which conserves vorticity and kinetic energy (so both (2.42) and (2.44) are satisfied) but does not conserve enstrophy.

Averaging the orographic term over the same region yields

$$\left[\nabla_H \cdot \left(\mathbf{u}_\psi \ln D\right)\right]_{i,j} = A_{i,j}^{-1}(F_{i+1,j}^r - F_{i-1,j}^r + F_{i,j+1}^\theta - F_{i,j-1}^\theta), \tag{B.6}$$

where

$$F_{i,j}^r = U_{i,j} \int_{\theta_{j-1}}^{\theta_{j+1}} \ln D \,\mathrm{d}\theta \tag{B.7}$$

is the radial flux through the azimuthal arc $r = r_i$, $\theta_{j-1} \le \theta \le \theta_{j+1}$, and

$$F_{i,j}^\theta = v_{i,j} \int_{r_{i-1}}^{r_{i+1}} \ln D \,\mathrm{d}r \tag{B.8}$$

is the azimuthal flux through the radial line $r_{i-1} \le r \le r_{i+1}$, $\theta = \theta_j$, where we have neglected the variation in the velocity along the sides of each cell. The conventional

[1]discussion of the method used at the origin is deferred until the next section

approach is to approximate the integrals in (B.7) and (B.8) as $2\Delta_\theta[\ln D]_{i,j}$ and $2\Delta_r[\ln D]_{i,j}$, but this leads to errors in the fluxes, particularly in cells which straddle the ellipse joining the interior and sloping sidewall in the sliced cone where there is a discontinuous change in the depth gradient. These errors produce a long-wavelength perturbation to the flow due to the near-coincidence of the joining ellipse with grid circles. This numerical artefact is eliminated by using integrals of $\ln D$, as in (B.7) and (B.8). The integrals are independent of time, so they were evaluated once in the initialisation (using a Romberg integration method based on an extended midpoint rule from Press *et al.*, 1992) and stored. Since each flux is used in two computational cells, additional efficiency was obtained by storing the fluxes and reusing them within each timestep.

The lateral viscosity term was averaged over a smaller region, $r_{i-\frac{1}{2}} \leq r \leq r_{i+\frac{1}{2}}$, $\theta_{j-\frac{1}{2}} \leq \theta \leq \theta_{j+\frac{1}{2}}$, giving the second-order flux-conservative formula

$$\begin{aligned}
\left[\nabla_H^2 \zeta\right]_{i,j} &= 4A_{i,j}^{-1}\big[\ \ r_{i+\frac{1}{2}}\Delta_\theta\Delta_r^{-1}\left(\zeta_{i+1,j}-\zeta_{i,j}\right) \\
&\qquad -r_{i-\frac{1}{2}}\Delta_\theta\Delta_r^{-1}\left(\zeta_{i,j}-\zeta_{i-1,j}\right) \\
&\qquad +\Delta_r(r_i\Delta_\theta)^{-1}\left(\zeta_{i,j+1}-\zeta_{i,j}\right) \\
&\qquad -\Delta_r(r_i\Delta_\theta)^{-1}\left(\zeta_{i,j}-\zeta_{i,j-1}\right)\big] \\
&= (r_i\Delta_r\Delta_\theta)^{-1}\big[\ \ r_i\Delta_\theta\Delta_r^{-1}\left(\zeta_{i+1,j}-2\zeta_{i,j}+\zeta_{i-1,j}\right) \\
&\qquad +\frac{1}{2}\Delta_\theta\left(\zeta_{i+1,j}-\zeta_{i-1,j}\right) \\
&\qquad +\Delta_r(r_i\Delta_\theta)^{-1}\left(\zeta_{i,j+1}-2\zeta_{i,j}+\zeta_{i,j-1}\right)\big] \\
&= \ \ \Delta_r^{-2}\left(\zeta_{i+1,j}-2\zeta_{i,j}+\zeta_{i-1,j}\right) \\
&\qquad +(2r_i\Delta_r)^{-1}\left(\zeta_{i+1,j}-\zeta_{i-1,j}\right) \\
&\qquad +(r_i\Delta_\theta)^{-2}\left(\zeta_{i,j+1}-2\zeta_{i,j}+\zeta_{i,j-1}\right). \qquad \text{(B.9)}
\end{aligned}$$

The geometry in the sliced cone and sliced cylinder allows for some simplification of the slope correction to the Ekman pumping. On the sloping sidewall we have $\frac{\partial D}{\partial \theta} = 0$ and the Ekman pumping term in equation (2.33) has the form

$$(\mathfrak{E})_{i,j} = \frac{E^{\frac{1}{2}}}{2D_{i,j}}\left[\zeta_T - (1+\sigma)\zeta_{i,j} - \frac{s^2\sigma}{r_i^2}\left(\frac{\partial^2\psi}{\partial\theta^2}\right)_{i,j}\right], \qquad \text{(B.10)}$$

where $\frac{\partial^2\psi}{\partial\theta^2}$ was obtained by the second-order formula

$$\left(\frac{\partial^2\psi}{\partial\theta^2}\right)_{i,j} = \frac{\psi_{i,j+1}-2\psi_{i,j}+\psi_{i,j-1}}{\Delta_\theta^2}. \qquad \text{(B.11)}$$

With a 45° slope we have $s = 1$ and $\sigma = 2^{\frac{1}{4}}$, as used in GV98. In the interior of the sliced cone (and everywhere in the sliced cylinder) the bottom slope s is 0.1. Its effect on the bottom Ekman layer is negligible, so the Ekman pumping term was simplified to

$$(\mathfrak{E})_{i,j} = \frac{E^{\frac{1}{2}}}{2D_{i,j}}\left[\zeta_T - 2\zeta_{i,j}\right]. \qquad \text{(B.12)}$$

For efficiency, equation (B.10) was used in both regions, by setting $s = 0$ and $\sigma = 1$ in the non-slope region.

B.3 Temporal advancement

The discretised vorticity equation was advanced in time using the alternating-direction implicit method (ADI). This method is unconditionally stable for $Ro = 0$ (Page, 1982), allowing spatial and temporal resolutions to be chosen according to the physical scales of the problem without any CFL-type restrictions based on Rossby wave propagation times across grid cells[2]—this is particularly important in a polar grid due to the convergence of grid lines at the origin. The method also has second-order accuracy in time. The approach is to split each timestep into two equal half-steps, as shown in figure 2.2. In the first timestep implicit differences are used in one spatial direction ($\hat{\theta}$ in our case) and explicit differences are used in the other direction ($\hat{\mathbf{r}}$); in the second half-timestep the reverse is the case (explicit in $\hat{\theta}$, implicit in $\hat{\mathbf{r}}$). This technique provides the stability advantages of fully implicit schemes but is much more efficient because the implicit differences are one-dimensional in each half-timestep (in our case, the matrix problem is almost tridiagonal since second-order differences are used; the two off-tridiagonal elements are due to the cyclic nature of the index j).

We shall use superscripts to denote the timestep. Each timestep begins by estimating the values $\widetilde{\zeta}^{n+\frac{1}{2}}$, $\widetilde{\psi}^{n+\frac{1}{2}}$, $\widetilde{\zeta}^{n+1}$ and $\widetilde{\psi}^{n+1}$ of the fields at the end of each half-timestep, by linear extrapolation from steps $n-1$ and n. Corrections $\check{\zeta}^{n+\frac{1}{2}}$ and $\check{\zeta}^{n+1}$ are calculated by solving the vorticity equation by the ADI method (tildes will be used to indicate approximate values and inverted "hats" will indicate corrections). This method requires the value of $\check{\zeta}^{n+1}$ at the boundary for the implicit radial differences in the second half-timestep; this is unknown for no-slip boundary conditions and is obtained in this case by a relaxation method that minimises the velocity at the boundary. Once $\widetilde{\zeta}^{n+1}$ has been corrected, the Poisson equation (2.34) is solved for the corrected value of $\widetilde{\psi}^{n+1}$ by applying a fast Fourier transform in θ and solving the resulting (almost) tridiagonal system directly. Since ψ and ζ are coupled nonlinearly through the advection term in the vorticity equation, the calculations of ζ^{n+1} and ψ^{n+1} are iterated within each timestep until they converge. The relaxation of ζ^{n+1} at the boundary (for no-slip boundary conditions) is also accomplished as part of this in-timestep iteration.

B.3.1 The first half-timestep

For the first half-timestep we are effectively evaluating the vorticity equation at time $(n+\frac{1}{4})\Delta_t$, where Δ_t is the timestep. The exact value of ζ at timestep $n+\frac{1}{2}$ is $\zeta^{n+\frac{1}{2}} \approx \widetilde{\zeta}^{n+\frac{1}{2}} + \check{\zeta}^{n+\frac{1}{2}}$.

The time derivative for the first half-timestep is

$$\left(\frac{\partial \zeta}{\partial t}\right)_{i,j}^{n+\frac{1}{4}} = \widetilde{\left(\frac{\partial \zeta}{\partial t}\right)}_{i,j}^{n+\frac{1}{4}} + \frac{\check{\zeta}_{i,j}^{n+\frac{1}{2}}}{\frac{1}{2}\Delta_t}, \tag{B.13}$$

where

$$\widetilde{\left(\frac{\partial \zeta}{\partial t}\right)}_{i,j}^{n+\frac{1}{4}} = \frac{\widetilde{\zeta}_{i,j}^{n+\frac{1}{2}} - \zeta_{i,j}^{n}}{\frac{1}{2}\Delta_t}. \tag{B.14}$$

[2]For $Ro > 0$ a CFL-type restriction applies, based on the advective velocity. In the sliced cone and sliced cylinder this velocity is large near the boundary, rather than the origin

The first half-timestep is implicit in θ, so the advection term in the first half-timestep is

$$\left[\nabla_H \cdot (\mathbf{u}_\psi \zeta)\right]_{i,j}^{n+\frac{1}{4}} = \widetilde{\left[\nabla_H \cdot (\mathbf{u}_\psi \zeta)\right]}_{i,j}^{n+\frac{1}{4}} + 2A_{i,j}^{-1}\Delta_r \left(v_{i,j+1}^{n+\frac{1}{4}} \zeta_{i,j+1}^{n+\frac{1}{2}} - v_{i,j-1}^{n+\frac{1}{4}} \zeta_{i,j-1}^{n+\frac{1}{2}} \right), \tag{B.15}$$

where

$$\begin{aligned}\widetilde{\left[\nabla_H \cdot (\mathbf{u}_\psi \zeta)\right]}_{i,j}^{n+\frac{1}{4}} = 2A_{i,j}^{-1} \Big[\quad & \Delta_\theta \left(U_{i+1,j}^{n+\frac{1}{4}} \zeta_{i+1,j}^{n} - U_{i-1,j}^{n+\frac{1}{4}} \zeta_{i-1,j}^{n} \right) \\ & + \Delta_r \left(v_{i,j+1}^{n+\frac{1}{4}} \widetilde{\zeta}_{i,j+1}^{n+\frac{1}{2}} - v_{i,j-1}^{n+\frac{1}{4}} \widetilde{\zeta}_{i,j-1}^{n+\frac{1}{2}} \right) \Big],\end{aligned} \tag{B.16}$$

and the "velocities" are calculated at the same timestep as the corresponding vorticities:

$$U_{i,j}^{n+\frac{1}{4}} = -\left(\frac{\psi_{i,j+1}^{n} - \psi_{i,j-1}^{n}}{2\Delta_\theta} \right), \tag{B.17}$$

and

$$v_{i,j}^{n+\frac{1}{4}} = \frac{\widetilde{\psi}_{i+1,j}^{n+\frac{1}{2}} - \widetilde{\psi}_{i-1,j}^{n+\frac{1}{2}}}{2\Delta_r}. \tag{B.18}$$

The orographic term $\left[\nabla_H \cdot (\mathbf{u}_\psi \ln D)\right]_{i,j}^{n+\frac{1}{4}}$ retains the form in (B.6), using the "velocities" defined above. The vorticity in the Ekman term is evaluated at step $n + \frac{1}{4}$, so the value used is $\frac{1}{2}\left(\zeta_{i,j}^{n} + \widetilde{\zeta}_{i,j}^{n+\frac{1}{2}} + \zeta_{i,j}^{n+\frac{1}{2}} \right)$. The stretching term is therefore

$$\left[\frac{\partial w}{\partial z}\right]_{i,j}^{n+\frac{1}{4}} = \widetilde{\left[\frac{\partial w}{\partial z}\right]}_{i,j}^{n+\frac{1}{4}} - \frac{E^{\frac{1}{2}}}{4D_{i,j}}(1+\sigma)\zeta_{i,j}^{n+\frac{1}{2}}, \tag{B.19}$$

where

$$\widetilde{\left[\frac{\partial w}{\partial z}\right]}_{i,j}^{n+\frac{1}{4}} = \left[\nabla_H \cdot (\mathbf{u}_\psi \ln D)\right]_{i,j}^{n+\frac{1}{4}} + \frac{E^{\frac{1}{2}}}{2D_{i,j}} \left[\zeta_T - (1+\sigma)\frac{\zeta_{i,j}^{n} + \widetilde{\zeta}_{i,j}^{n+\frac{1}{2}}}{2} - \frac{\sigma s^2}{r_i^2} \left(\frac{\partial^2 \psi}{\partial \theta^2} \right)_{i,j}^{n+\frac{1}{4}} \right], \tag{B.20}$$

$$\left(\frac{\partial^2 \psi}{\partial \theta^2} \right)_{i,j}^{n+\frac{1}{4}} = \frac{\psi_{i,j+1}^{n} - 2\psi_{i,j}^{n} + \psi_{i,j-1}^{n}}{\Delta_\theta^2}, \tag{B.21}$$

and we neglect the insignificant correction to the Ekman pumping in the sliced cylinder and the interior of the sliced cone by setting $s = 0$, $\sigma = 1$ in these regions.

The viscous term in the first half-timestep is

$$\left[\nabla_H^2 \zeta\right]_{i,j}^{n+\frac{1}{4}} = \widetilde{\left[\nabla_H^2 \zeta\right]}_{i,j}^{n+\frac{1}{4}} + (r_i \Delta_\theta)^{-2} \left(\zeta_{i,j+1}^{n+\frac{1}{2}} - 2\zeta_{i,j}^{n+\frac{1}{2}} + \zeta_{i,j-1}^{n+\frac{1}{2}} \right), \tag{B.22}$$

where

$$\begin{aligned}\widetilde{\left[\nabla_H^2 \zeta\right]}_{i,j}^{n+\frac{1}{4}} = \quad & \Delta_r^{-2} \left(\zeta_{i+1,j}^{n} - 2\zeta_{i,j}^{n} + \zeta_{i-1,j}^{n} \right) \\ & + (2r_i \Delta_r)^{-1} \left(\zeta_{i+1,j}^{n} - \zeta_{i-1,j}^{n} \right) \\ & + (r_i \Delta_\theta)^{-2} \left(\widetilde{\zeta}_{i,j+1}^{n+\frac{1}{2}} - 2\widetilde{\zeta}_{i,j}^{n+\frac{1}{2}} + \widetilde{\zeta}_{i,j-1}^{n+\frac{1}{2}} \right).\end{aligned} \tag{B.23}$$

Using these terms, at $(n+\frac{1}{4})\Delta_t$ the vorticity equation (2.33) becomes

$$\begin{aligned}
&Ro\widetilde{\left[\frac{\partial\zeta}{\partial t}\right]}_{i,j}^{n+\frac{1}{4}} + Ro\left[\nabla_H\cdot\widetilde{(\mathbf{u}_\psi\zeta)}\right]_{i,j}^{n+\frac{1}{4}} - 2\widetilde{\left[\frac{\partial w}{\partial z}\right]}_{i,j}^{n+\frac{1}{4}} - E\widetilde{\left[\nabla_H^2\zeta\right]}_{i,j}^{n+\frac{1}{4}} \\
&= -Ro\frac{\breve{\zeta}_{i,j}^{n+\frac{1}{2}}}{\frac{1}{2}\Delta_t} - 2RoA_{i,j}^{-1}\Delta_r\left(v_{i,j+1}^{n+\frac{1}{4}}\breve{\zeta}_{i,j+1}^{n+\frac{1}{2}} - v_{i,j-1}^{n+\frac{1}{4}}\breve{\zeta}_{i,j-1}^{n+\frac{1}{2}}\right) \\
&\quad - \frac{E^{\frac{1}{2}}}{2D_{i,j}}(1+\sigma)\breve{\zeta}_{i,j}^{n+\frac{1}{2}} + E(r_i\Delta_\theta)^{-2}\left(\breve{\zeta}_{i,j+1}^{n+\frac{1}{2}} - 2\breve{\zeta}_{i,j}^{n+\frac{1}{2}} + \breve{\zeta}_{i,j-1}^{n+\frac{1}{2}}\right) \\
&= \quad a_{i,j}^{n+\frac{1}{4}}\breve{\zeta}_{i,j-1}^{n+\frac{1}{2}} + b_{i,j}^{n+\frac{1}{4}}\breve{\zeta}_{i,j}^{n+\frac{1}{2}} + c_{i,j}^{n+\frac{1}{4}}\breve{\zeta}_{i,j+1}^{n+\frac{1}{2}},
\end{aligned} \tag{B.24}$$

where

$$a_{i,j}^{n+\frac{1}{4}} = 2RoA_{i,j}^{-1}\Delta_r v_{i,j-1}^{n+\frac{1}{4}} + E(r_i\Delta_\theta)^{-2}, \tag{B.25}$$

$$b_{i,j}^{n+\frac{1}{4}} = -2Ro\Delta_t^{-1} - \frac{E^{\frac{1}{2}}}{2D_{i,j}}(1+\sigma) - 2E(r_i\Delta_\theta)^{-2} \tag{B.26}$$

and

$$c_{i,j}^{n+\frac{1}{4}} = -2RoA_{i,j}^{-1}\Delta_r v_{i,j+1}^{n+\frac{1}{4}} + E(r_i\Delta_\theta)^{-2}. \tag{B.27}$$

The solution of this algebraic equation for $\breve{\zeta}^{n+\frac{1}{2}}$ is complicated slightly by the cyclic nature of j, so this system is not quite tridiagonal. It can nevertheless be solved efficiently using a slightly modified version of the standard tridiagonal inversion algorithm.

After the correction $\breve{\zeta}^{n+\frac{1}{2}}$ has been found for the interior points[3] it needs to be calculated at the origin. For this grid-point the advection, orographic and viscous terms are evaluated in terms of fluxes through the boundary of a circle centred on the origin, with the fluxes matched to those in the interior cells. The advection term is calculated by averaging over the disk $r \leq r_1$, giving

$$\left[\nabla_H\cdot\widetilde{(\mathbf{u}_\psi\zeta)}\right]_{0,j}^{n+\frac{1}{4}} = \frac{2}{N_j r_1^2}\sum_{j=1}^{N_j} U_{1,j}^{n+\frac{1}{4}}\zeta_{1,j}^n. \tag{B.28}$$

The orographic term is averaged over the same disk, so

$$\left[\nabla_H\cdot\widetilde{(\mathbf{u}_\psi\ln D)}\right]_{0,j}^{n+\frac{1}{4}} = \frac{1}{2\pi r_1^2}\sum_{j=1}^{N_j} F_{1,j}^{r,n+\frac{1}{4}}, \tag{B.29}$$

where the factor of $\frac{1}{2}$ occurs because the fluxes $F_{i,j}^r$ are integrals over $2\Delta_\theta$. The viscous term is averaged over the smaller disk $r \leq r_{\frac{1}{2}}$, which yields

$$\widetilde{\left[\nabla_H^2\zeta\right]}_{0,j}^{n+\frac{1}{4}} = \frac{4}{N_j r_1^2}\sum_{j=1}^{N_j}\left(\zeta_{1,j}^n - \zeta_{0,j}^n\right). \tag{B.30}$$

[3] $\breve{\zeta}^{n+\frac{1}{2}}$ is not calculated at the boundary at this stage, since it is not needed in the second half-timestep.

The expressions for the time derivative and Ekman dissipation are the same as those used in the rest of the interior; these are the only terms in which the correction $\breve{\zeta}_{0,j}^{n+\frac{1}{4}}$ appears. The stretching term $\widetilde{\left[\frac{\partial w}{\partial z}\right]}_{0,j}^{n+\frac{1}{4}}$ has the same form as elsewhere in the interior, apart from the different expression for the orographic term. Substituting these terms into the vorticity equation (2.33) yields an expression for $\breve{\zeta}_{0,j}^{n+\frac{1}{4}}$:

$$\breve{\zeta}_{0,j}^{n+\frac{1}{4}} = \frac{-1}{2Ro\Delta_t^{-1} + E^{\frac{1}{2}} D_{0,j}^{-1}} \left\{ Ro\widetilde{\left[\frac{\partial \zeta}{\partial t}\right]}_{0,j}^{n+\frac{1}{4}} + Ro\widetilde{\left[\nabla_H \cdot (\mathbf{u}_\psi \zeta)\right]}_{0,j}^{n+\frac{1}{4}} - 2\widetilde{\left[\frac{\partial w}{\partial z}\right]}_{0,j}^{n+\frac{1}{4}} - E\widetilde{\left[\nabla_H^2 \zeta\right]}_{0,j}^{n+\frac{1}{4}} \right\}, \tag{B.31}$$

where we have again neglected the correction to the Ekman pumping by setting $s = 0$ and $\sigma = 1$.

At the end of the first half-timestep the vorticity values at $n+\frac{1}{2}$ are corrected: $\zeta_{i,j}^{n+\frac{1}{2}} \leftarrow \widetilde{\zeta}_{i,j}^{n+\frac{1}{2}} + \breve{\zeta}_{i,j}^{n+\frac{1}{2}}$. For efficiency, the corrected vorticity is not used to correct $\widetilde{\psi}_{i,j}^{n+\frac{1}{2}}$, so the Poisson equation (2.34) is not satisfied exactly at this stage. The Poisson equation is solved at the end of the second half-timestep, ensuring that this error remains small.

B.3.2 The second half-timestep

For the second half-timestep we are effectively evaluating the vorticity equation at time $(n+\frac{3}{4})\Delta_t$. The exact value of ζ at timestep $n+1$ is $\zeta^{n+1} \approx \widetilde{\zeta}^{n+1} + \breve{\zeta}^{n+1}$.

The time derivative for the second half-timestep is

$$\left(\frac{\partial \zeta}{\partial t}\right)_{i,j}^{n+\frac{3}{4}} = \widetilde{\left(\frac{\partial \zeta}{\partial t}\right)}_{i,j}^{n+\frac{3}{4}} + \frac{\breve{\zeta}_{i,j}^{n+1}}{\frac{1}{2}\Delta_t}, \tag{B.32}$$

where

$$\widetilde{\left(\frac{\partial \zeta}{\partial t}\right)}_{i,j}^{n+\frac{3}{4}} = \frac{\widetilde{\zeta}_{i,j}^{n+1} - \zeta_{i,j}^{n+\frac{1}{2}}}{\frac{1}{2}\Delta_t}. \tag{B.33}$$

The second half-timestep is implicit in r, so the advection term in the second half-timestep is

$$\left[\nabla_H \cdot (\mathbf{u}_\psi \zeta)\right]_{i,j}^{n+\frac{3}{4}} = \widetilde{\left[\nabla_H \cdot (\mathbf{u}_\psi \zeta)\right]}_{i,j}^{n+\frac{3}{4}} + 2A_{i,j}^{-1}\Delta_\theta \left(U_{i+1,j}^{n+\frac{3}{4}} \breve{\zeta}_{i+1,j}^{n+1} - U_{i-1,j}^{n+\frac{3}{4}} \breve{\zeta}_{i-1,j}^{n+1} \right), \tag{B.34}$$

where

$$\begin{aligned} \widetilde{\left[\nabla_H \cdot (\mathbf{u}_\psi \zeta)\right]}_{i,j}^{n+\frac{3}{4}} = 2A_{i,j}^{-1} \Big[& \Delta_\theta \left(U_{i+1,j}^{n+\frac{3}{4}} \widetilde{\zeta}_{i+1,j}^{n+1} - U_{i-1,j}^{n+\frac{3}{4}} \widetilde{\zeta}_{i-1,j}^{n+1} \right) \\ & + \Delta_r \left(v_{i,j+1}^{n+\frac{3}{4}} \zeta_{i,j+1}^{n+\frac{1}{2}} - v_{i,j-1}^{n+\frac{3}{4}} \zeta_{i,j-1}^{n+\frac{1}{2}} \right) \Big], \end{aligned} \tag{B.35}$$

and the "velocities" are calculated at the same timestep as the corresponding vorticities:

$$U_{i,j}^{n+\frac{3}{4}} = -\left(\frac{\widetilde{\psi}_{i,j+1}^{n+1} - \widetilde{\psi}_{i,j-1}^{n+1}}{2\Delta_\theta} \right), \tag{B.36}$$

and

$$v_{i,j}^{n+\frac{3}{4}} = \frac{\widetilde{\psi}_{i+1,j}^{n+\frac{1}{2}} - \widetilde{\psi}_{i-1,j}^{n+\frac{1}{2}}}{2\Delta_r} = v_{i,j}^{n+\frac{1}{4}}. \tag{B.37}$$

The orographic term $\left[\nabla_H \cdot \left(\mathbf{u}_\psi \ln D\right)\right]_{i,j}^{n+\frac{3}{4}}$ retains the form in (B.6), using the "velocities" defined above. The vorticity in the Ekman term is evaluated at step $n + \frac{3}{4}$, so the value used is $\frac{1}{2}\left(\zeta_{i,j}^{n+\frac{1}{2}} + \widetilde{\zeta}_{i,j}^{n+1} + \check{\zeta}_{i,j}^{n+1}\right)$. The stretching term is therefore

$$\left[\frac{\partial w}{\partial z}\right]_{i,j}^{n+\frac{3}{4}} = \widetilde{\left[\frac{\partial w}{\partial z}\right]}_{i,j}^{n+\frac{3}{4}} - \frac{E^{\frac{1}{2}}}{4D_{i,j}}(1+\sigma)\check{\zeta}_{i,j}^{n+1}, \tag{B.38}$$

where

$$\widetilde{\left[\frac{\partial w}{\partial z}\right]}_{i,j}^{n+\frac{3}{4}} = \left[\nabla_H \cdot \left(\mathbf{u}_\psi \ln D\right)\right]_{i,j}^{n+\frac{3}{4}} + \frac{E^{\frac{1}{2}}}{2D_{i,j}}\left[\zeta_T - (1+\sigma)\frac{\zeta_{i,j}^{n+\frac{1}{2}} + \widetilde{\zeta}_{i,j}^{n+1}}{2} - \frac{\sigma s^2}{r_i^2}\left(\frac{\partial^2\psi}{\partial\theta^2}\right)_{i,j}^{n+\frac{3}{4}}\right], \tag{B.39}$$

$$\left(\frac{\partial^2\psi}{\partial\theta^2}\right)_{i,j}^{n+\frac{3}{4}} = \frac{\widetilde{\psi}_{i,j+1}^{n+1} - 2\widetilde{\psi}_{i,j}^{n+1} + \widetilde{\psi}_{i,j-1}^{n+1}}{\Delta_\theta^2}, \tag{B.40}$$

and we neglect the insignificant correction to the Ekman pumping in the sliced cylinder and the interior of the sliced cone by setting $s = 0$, $\sigma = 1$ in these regions.

The viscous term in the second half-timestep is

$$\begin{aligned} \left[\nabla_H^2\zeta\right]_{i,j}^{n+\frac{3}{4}} = & \widetilde{\left[\nabla_H^2\zeta\right]}_{i,j}^{n+\frac{3}{4}} \\ & + \Delta_r^{-2}\left(\check{\zeta}_{i+1,j}^{n+1} - 2\check{\zeta}_{i,j}^{n+1} + \check{\zeta}_{i-1,j}^{n+1}\right) \\ & + (2r_i\Delta_r)^{-1}\left(\check{\zeta}_{i+1,j}^{n+1} - \check{\zeta}_{i-1,j}^{n+1}\right), \end{aligned} \tag{B.41}$$

where

$$\begin{aligned} \widetilde{\left[\nabla_H^2\zeta\right]}_{i,j}^{n+\frac{3}{4}} = & \Delta_r^{-2}\left(\widetilde{\zeta}_{i+1,j}^{n+1} - 2\widetilde{\zeta}_{i,j}^{n+1} + \widetilde{\zeta}_{i-1,j}^{n+1}\right) \\ & + (2r_i\Delta_r)^{-1}\left(\widetilde{\zeta}_{i+1,j}^{n+1} - \widetilde{\zeta}_{i-1,j}^{n+1}\right) \\ & + (r_i\Delta_\theta)^{-2}\left(\zeta_{i,j+1}^{n+\frac{1}{2}} - 2\zeta_{i,j}^{n+\frac{1}{2}} + \zeta_{i,j-1}^{n+\frac{1}{2}}\right). \end{aligned} \tag{B.42}$$

Using these terms, at $(n+\frac{3}{4})\Delta_t$ the vorticity equation (2.33) becomes

$$
\begin{aligned}
&Ro\widetilde{\left[\frac{\partial\zeta}{\partial t}\right]}_{i,j}^{n+\frac{3}{4}} + Ro\big[\nabla_H\cdot\widetilde{(\mathbf{u}_\psi\zeta)}\big]_{i,j}^{n+\frac{3}{4}} - 2\widetilde{\left[\frac{\partial w}{\partial z}\right]}_{i,j}^{n+\frac{3}{4}} - E\widetilde{\left[\nabla_H^2\zeta\right]}_{i,j}^{n+\frac{3}{4}} \\
&= - Ro\frac{\check{\zeta}_{i,j}^{n+1}}{\frac{1}{2}\Delta_t} - 2RoA_{i,j}^{-1}\Delta_\theta\left(U_{i+1,j}^{n+\frac{3}{4}}\check{\zeta}_{i+1,j}^{n+1} - U_{i-1,j}^{n+\frac{3}{4}}\check{\zeta}_{i-1,j}^{n+1}\right) \\
&\quad - \frac{E^{\frac{1}{2}}}{2D_{i,j}}(1+\sigma)\check{\zeta}_{i,j}^{n+1} + E\Delta_r^{-2}\left(\check{\zeta}_{i+1,j}^{n+1} - 2\check{\zeta}_{i,j}^{n+1} + \check{\zeta}_{i-1,j}^{n+1}\right) \\
&\quad + E(2r_i\Delta_r)^{-1}\left(\check{\zeta}_{i+1,j}^{n+1} - \check{\zeta}_{i-1,j}^{n+1}\right) \\
&= \quad a_{i,j}^{n+\frac{3}{4}}\check{\zeta}_{i-1,j}^{n+1} + b_{i,j}^{n+\frac{3}{4}}\check{\zeta}_{i,j}^{n+1} + c_{i,j}^{n+\frac{3}{4}}\check{\zeta}_{i+1,j}^{n+1},
\end{aligned}
\tag{B.43}
$$

where

$$a_{i,j}^{n+\frac{3}{4}} = 2RoA_{i,j}^{-1}\Delta_\theta U_{i-1,j}^{n+\frac{3}{4}} + E\Delta_r^{-2} - E(2r_i\Delta_r)^{-1}, \tag{B.44}$$

$$b_{i,j}^{n+\frac{3}{4}} = -2Ro\Delta_t^{-1} - \frac{E^{\frac{1}{2}}}{2D_{i,j}}(1+\sigma) - 2E\Delta_r^{-2} \tag{B.45}$$

and

$$c_{i,j}^{n+\frac{3}{4}} = -2RoA_{i,j}^{-1}\Delta_\theta U_{i+1,j}^{n+\frac{3}{4}} + E\Delta_r^{-2} + E(2r_i\Delta_r)^{-1}. \tag{B.46}$$

The solution of this linear equation for $\check{\zeta}^{n+1}$ requires $\check{\zeta}_{N_i,j}^{n+1}$, which is known for free-slip boundary conditions (2.40) (or super-slip boundary conditions (2.41) in the sliced cone) but is unknown for no-slip conditions (2.39). In this case $\check{\zeta}_{N_i,j}^{n+1}$ is found by an optimal relaxation method described by Page (1981). The solution of this linear system also requires $\check{\zeta}_{0,j}^{n+1}$, which is not yet known. We can solve the latter difficulty by writing $\check{\zeta}_{i,j}^{n+1} = \widetilde{\check{\zeta}_{i,j}^{n+1}} + \left(\partial\check{\zeta}^{n+1}/\partial\check{\zeta}_{0,j}^{n+1}\right)_{i,j}\check{\zeta}_{0,j}^{n+1}$; we can solve for $\widetilde{\check{\zeta}_{i,j}^{n+1}}$ and $\left(\partial\check{\zeta}^{n+1}/\partial\check{\zeta}_{0,j}^{n+1}\right)_{i,j}$ before $\check{\zeta}_{0,j}^{n+1}$ is known, then use $\left(\partial\check{\zeta}^{n+1}/\partial\check{\zeta}_{0,j}^{n+1}\right)_{i,j}$ to find $\check{\zeta}_{i,j}^{n+1}$ after $\check{\zeta}_{0,j}^{n+1}$ has been calculated.

The matrix in (B.43) is decomposed into a product of upper- and lower-triangular matrices by writing

$$\check{\zeta}_{i,j}^{n+1} = L_{i,j} + M_{i,j}\check{\zeta}_{i+1,j}^{n+1} + N_{i,j}\check{\zeta}_{0,j}^{n+1}. \tag{B.47}$$

Substituting this expression into (B.43) implies

$$L_{i,j} = \frac{Ro\widetilde{\left[\frac{\partial\zeta}{\partial t}\right]}_{i,j}^{n+\frac{3}{4}} + Ro\big[\nabla_H\cdot\widetilde{(\mathbf{u}_\psi\zeta)}\big]_{i,j}^{n+\frac{3}{4}} - 2\widetilde{\left[\frac{\partial w}{\partial z}\right]}_{i,j}^{n+\frac{3}{4}} - E\widetilde{\left[\nabla_H^2\zeta\right]}_{i,j}^{n+\frac{3}{4}} - a_{i,j}L_{i-1,j}}{a_{i,j}M_{i-1,j} + b_{i,j}}, \tag{B.48}$$

$$M_{i,j} = \frac{-c_{i,j}}{a_{i,j}M_{i-1,j} + b_{i,j}}, \tag{B.49}$$

and

$$N_{i,j} = \frac{-a_{i,j}N_{i-1,j}}{a_{i,j}M_{i-1,j} + b_{i,j}}. \tag{B.50}$$

These coefficients can be found recursively, starting from $L_{0,j} = 0$, $M_{0,j} = 0$ and $N_{0,j} = 1$. Direct back-substitution via (B.47) cannot proceed until $\check{\zeta}_{0,j}^{n+1}$ is known, but calculation of $\check{\zeta}_{0,j}^{n+1}$ requires the values of $\check{\zeta}_{1,j}^{n+1}$. The solution to this dilemma is to write

$$\check{\zeta}_{i,j}^{n+1} = \widetilde{\check{\zeta}_{i,j}^{n+1}} + \left(\frac{\partial \check{\zeta}^{n+1}}{\partial \check{\zeta}_{0,j}^{n+1}}\right)_{i,j} \check{\zeta}_{0,j}^{n+1}, \tag{B.51}$$

where

$$\widetilde{\check{\zeta}_{i,j}^{n+1}} = L_{i,j} + M_{i,j}\widetilde{\check{\zeta}_{i+1,j}^{n+1}}, \tag{B.52}$$

which allows us to solve for $\widetilde{\check{\zeta}_{i,j}^{n+1}}$ by back-substitution, since the boundary value $\widetilde{\check{\zeta}_{N_i,j}^{n+1}} = \check{\zeta}_{N_i,j}^{n+1}$ is given by relaxation. Combining (B.47), (B.51), and (B.52) yields the formula

$$\left(\frac{\partial \check{\zeta}^{n+1}}{\partial \check{\zeta}_{0,j}^{n+1}}\right)_{i,j} = N_{i,j} + M_{i,j}\left(\frac{\partial \check{\zeta}^{n+1}}{\partial \check{\zeta}_{0,j}^{n+1}}\right)_{i+1,j}, \tag{B.53}$$

which gives $\left(\partial \check{\zeta}^{n+1}/\partial \check{\zeta}_{0,j}^{n+1}\right)_{i,j}$ by back-substitution, given that $\left(\partial \check{\zeta}^{n+1}/\partial \check{\zeta}_{0,j}^{n+1}\right)_{N_i,j} = 0$ at the boundary because $\check{\zeta}_{N_i,j}^{n+1}$ is determined by the boundary conditions.

After $\widetilde{\check{\zeta}_{i,j}^{n+1}}$ and $\left(\partial \check{\zeta}^{n+1}/\partial \check{\zeta}_{0,j}^{n+1}\right)_{i,j}$ have been found for the interior points, $\check{\zeta}_{0,j}^{n+1}$ needs to be calculated at the origin. As in the previous half-timestep the advection, orographic and viscous terms are evaluated in terms of fluxes through the boundary of a circle centred on the origin, with the fluxes matched to those in the interior cells. The advection term is calculated by averaging over the disk $r \leq r_1$, giving

$$\left[\nabla_H \cdot (\mathbf{u}_\psi \zeta)\right]_{0,j}^{n+\frac{3}{4}} = \left[\widetilde{\nabla_H \cdot (\mathbf{u}_\psi \zeta)}\right]_{0,j}^{n+\frac{3}{4}} + \frac{2\check{\zeta}_{0,j}^{n+1}}{N_j r_1^2}\sum_{j=1}^{N_j} U_{1,j}^{n+\frac{3}{4}}\left(\frac{\partial \check{\zeta}^{n+1}}{\partial \check{\zeta}_{0,j}^{n+1}}\right)_{1,j}, \tag{B.54}$$

where

$$\left[\widetilde{\nabla_H \cdot (\mathbf{u}_\psi \zeta)}\right]_{0,j}^{n+\frac{3}{4}} = \frac{2}{N_j r_1^2}\sum_{j=1}^{N_j} U_{1,j}^{n+\frac{3}{4}}\left[\tilde{\zeta}_{1,j}^{n+1} + \widetilde{\check{\zeta}_{1,j}^{n+1}}\right]. \tag{B.55}$$

The orographic term is averaged over the same disk, so

$$\left[\widetilde{\nabla_H \cdot (\mathbf{u}_\psi \ln D)}\right]_{0,j}^{n+\frac{3}{4}} = \frac{1}{2\pi r_1^2}\sum_{j=1}^{N_j} F_{1,j}^{r,n+\frac{3}{4}} = \left[\widetilde{\nabla_H \cdot (\mathbf{u}_\psi \ln D)}\right]_{0,j}^{n+\frac{1}{4}}. \tag{B.56}$$

The viscous term is averaged over the smaller disk $r \leq r_{\frac{1}{2}}$, which yields

$$\left[\nabla_H^2 \zeta\right]_{0,j}^{n+\frac{3}{4}} = \widetilde{\left[\nabla_H^2 \zeta\right]}_{0,j}^{n+\frac{3}{4}} + \frac{4\check{\zeta}_{0,j}^{n+1}}{N_j r_1^2}\sum_{j=1}^{N_j}\left[\left(\frac{\partial \check{\zeta}^{n+1}}{\partial \check{\zeta}_{0,j}^{n+1}}\right)_{1,j} - 1\right], \tag{B.57}$$

where

$$\widetilde{\left[\nabla_H^2 \zeta\right]}_{0,j}^{n+\frac{3}{4}} = \frac{4}{N_j r_1^2}\sum_{j=1}^{N_j}\left(\tilde{\zeta}_{1,j}^{n+1} + \widetilde{\check{\zeta}_{1,j}^{n+1}} - \tilde{\zeta}_{0,j}^{n+1}\right). \tag{B.58}$$

The expressions for the time derivative and Ekman dissipation are the same as those used in the rest of the interior. The stretching term $\widetilde{\left[\frac{\partial w}{\partial z}\right]}_{0,j}^{n+\frac{3}{4}}$ has the same form as elsewhere in the interior, apart from the different expression for the orographic term. Substituting these terms into the vorticity equation (2.33) yields an expression for $\check{\zeta}_{0,j}^{n+\frac{3}{4}}$:

$$\check{\zeta}_{0,j}^{n+\frac{3}{4}} = \frac{-Ro\widetilde{\left[\frac{\partial \zeta}{\partial t}\right]}_{0,j}^{n+\frac{3}{4}} - Ro\widetilde{\left[\nabla_H \cdot (\mathbf{u}_\psi \zeta)\right]}_{0,j}^{n+\frac{3}{4}} + 2\widetilde{\left[\frac{\partial w}{\partial z}\right]}_{0,j}^{n+\frac{3}{4}} + E\widetilde{\left[\nabla_H^2 \zeta\right]}_{0,j}^{n+\frac{3}{4}}}{2Ro\Delta_t^{-1} + \frac{2Ro}{N_j r_1^2}\sum_{j=1}^{N_j} U_{1,j}^{n+\frac{3}{4}}\left(\frac{\partial \check{\zeta}^{n+1}}{\partial \check{\zeta}_{0,j}^{n+1}}\right)_{1,j} + \frac{E^{\frac{1}{2}}}{D_{0,j}} - \frac{4E}{N_j r_1^2}\sum_{j=1}^{N_j}\left[\left(\frac{\partial \check{\zeta}^{n+1}}{\partial \check{\zeta}_{0,j}^{n+1}}\right)_{1,j} - 1\right]}, \tag{B.59}$$

where we have again neglected the correction to the Ekman pumping by setting $s = 0$ and $\sigma = 1$.

At the end of the second half-timestep the vorticity values at $n + 1$ are corrected: $\zeta_{i,j}^{n+1} \leftarrow \tilde{\zeta}_{i,j}^{n+1} + \widetilde{\check{\zeta}_{i,j}^{n+1}} + \left(\partial \check{\zeta}^{n+1}/\partial \check{\zeta}_{0,j}^{n+1}\right)_{i,j} \check{\zeta}_{0,j}^{n+1}$. The corrected vorticity is used to correct $\psi_{i,j}^{n+1}$ by solving the Poisson equation (2.34); this is also used to update the estimate of $\psi^{n+\frac{1}{2}}$. If the corrections are larger than a given tolerance, the two half-timesteps are repeated in order to refine the accuracy of the solution; otherwise the new values $\zeta_{i,j}^{n+1}$ and $\psi_{i,j}^{n+1}$ are used for the start of the next timestep (see figure 2.2).

Appendix C

Glossary of symbols

All symbols denote dimensionless quantities (length, time and velocity scaled by H_o, $|\epsilon\Omega|^{-1}$ and $|\epsilon\Omega|H_o$, respectively), unless otherwise stated.

Symbol	Description	See
a	Dimensional radius of basin	Fig. 2.1, p.11
$\mathtt{A}$	Advection term in ζ equation, $\mathtt{A} = -Ro\nabla_H \cdot \left(\mathbf{u}_\psi \zeta\right)$	p.83
D	Depth, $D = 1 - h$	p.15
D_{eff}	"Effective depth", $D_{\mathit{eff}} = e^{-Q/2} = De^{-Ro\zeta/2}$	Eq. (2.36), p.23
$\frac{\partial D_{\mathit{eff}}}{\partial S}$	Change in D_{eff} per unit arc length S along a streamline, $\frac{\partial D_{\mathit{eff}}}{\partial S} = (\mathbf{u}_\psi/\lvert\mathbf{u}_\psi\rvert) \cdot \nabla_H D_{\mathit{eff}}$	Eq. (5.5), p.99
E	Ekman number, $E = \frac{\nu}{\Omega H_o^2}$	p.13
$\mathtt{E}$	Ekman friction term in ζ equation, $\mathtt{E} = 2\mathfrak{E} - \mathtt{W}$	p.83
$\mathfrak{E}$	Stretching due to Ekman pumping	Eq. (2.32), p.22
$F^r_{i,j}$	Radial flux of $u(r_i,\theta)\ln D$ through the azimuthal arc $r = r_i$, $\theta_{j-1} \le \theta \le \theta_j$	Eq. (B.7), p.131
$F^\theta_{i,j}$	Azimuthal flux of $v(r,\theta_j)\ln D$ through the radial line $r_{i-1} \le r \le r_i$, $\theta = \theta_j$	Eq. (B.8), p.131
h	z-coordinate of bottom boundary	p.13
H_o	Dimensional depth at centre of basin	Fig. 2.1, p.11
i	Radial grid index	p.131
j	Azimuthal grid index	p.131
$\hat{\mathbf{k}}$	Vertical unit vector	p.11
K	Basin-integrated horizontal kinetic energy per unit depth	Eq. (2.45), p.26
$\mathtt{O}$	Orographic term in ζ equation, $\mathtt{O} = 2\nabla_H \cdot \left(\mathbf{u}_\psi \ln D\right)$	p.83
p	Pressure, with the hydrostatic component subtracted	p.13
Q	"Potential vorticity", $Q = -2\ln D_{\mathit{eff}} = Ro\zeta - 2\ln D$	Eq. (2.35), p.23
r	Radial coordinate	
$\hat{\mathbf{r}}$	Radial unit vector	p.130
r_e	Radial coordinate of join between interior and slope of sliced cone	Eq. (2.3), p.13
$r_{e_{max}}$	Maximum value of r_e	p.13
Re_γ	Western boundary current Reynolds number, $Re_\gamma = 2RoE^{-\frac{2}{3}}\Lambda s^{\frac{1}{3}}$	p.35
r_i	Radial coordinate at grid index i, $r_i = i\Delta_r$	p.131
Ro	Rossby number, $Ro = \lvert\epsilon\rvert$	p.13

Symbol	Description	See
s	Bottom slope, $s = \lvert\nabla_H h\rvert$	p.15
$\hat{\mathbf{s}}$	Unit vector in the direction of increasing h, $\hat{\mathbf{s}} = s^{-1}\nabla_H h$	p.15
s_{cr}	Bottom slope at which Stommel and Stewartson $E^{\frac{1}{4}}$ layers merge, $s_{cr} = (2/3)^{\frac{3}{2}}E^{\frac{1}{4}}$	p.19
s_i	Bottom slope s in the interior of the sliced cone	p.13
s_s	Slope s of the sidewall in the sliced cone	p.13
$\mathtt{T}$	Local rate of change in ζ equation, $\mathtt{T} = -Ro\frac{\partial\zeta}{\partial t}$	p.83
u	Eastward velocity (except in Appendices A and B)	
$\mathbf{u}$	Velocity vector, $\mathbf{u} = \mathbf{u}_H + \hat{\mathbf{k}}w$	p.13
$\mathbf{u}_0, \mathbf{u}_1, \ldots$	Velocity vector expanded in powers of $E^{\frac{1}{2}}$; $\mathbf{u} = \sum_{i=0}^{\infty} E^{\frac{i}{2}}\mathbf{u}_i$	p.14
$\mathbf{u}_{D_{\mathit{eff}}}$	"Velocity" vector along D_{eff} contours, $\mathbf{u}_{D_{\mathit{eff}}} = -\hat{\mathbf{k}} \times \nabla_H D_{\mathit{eff}}$	Eq. (5.2), p.90
$\mathbf{u}_H$	Horizontal velocity vector, $\mathbf{u}_H = \hat{\mathbf{k}} \times \nabla_H\psi + \nabla_H\phi$	p.13
$\mathbf{u}_\psi$	Nondivergent horizontal velocity, $\mathbf{u}_\psi = \hat{\mathbf{k}} \times \nabla_H\psi$	p.13
U	Radial flux per radian, $U = -\frac{\partial\psi}{\partial\theta}$	p.131
v	Northward velocity (except in Appendices A and B)	
v_{Sv}	Sverdrup northward velocity, $v_{Sv} = E^{\frac{1}{2}}\zeta_T/(2s)$	p.18
$\mathtt{V}$	Lateral viscous dissipation term in ζ equation, $\mathtt{V} = E\nabla_H^2\zeta$	p.83
w	Vertical velocity	p.13
w_T	Vertical velocity at the lid	Eq. (2.15), p.15
w_B	Vertical velocity at the bottom	Eq. (2.16), p.15
$\mathtt{W}$	"Wind" forcing term in ζ equation, $\mathtt{W} = \frac{E^{\frac{1}{2}}}{D}\zeta_T$	p.83
x	Coordinate pointing "east" (except in Appendix A)	Fig. 2.1, p.11
y	Coordinate pointing "north" (except in Appendix A)	Fig. 2.1, p.11
z	Coordinate pointing vertically upwards	Fig. 2.1, p.11
δ_I	Inertial WBC thickness, $\delta_I = (-Ro\, u_{int}/2s)^{\frac{1}{2}}$	p.30
δ_M	Munk WBC thickness, $\delta_M = (4E/s)^{\frac{1}{3}}$	p.19
δ_S	Stommel WBC thickness, $\delta_S = E^{\frac{1}{2}}/s$	p.19
$\Delta_{bal}, \Delta_{min}$	Thresholds for determining dominant terms in vorticity balance	p.83
Δ_r, Δ_θ	Grid spacings in radial and azimuthal directions	p.131
ϵ	Relative angular velocity of the lid	Fig. 2.1, p.11
ζ	Vertical component of the vorticity, $\zeta = \boldsymbol{\omega} \cdot \hat{\mathbf{k}}$	p.14
$\zeta_0, \zeta_1, \ldots$	ζ expanded in powers of $E^{\frac{1}{2}}$; $\zeta = \sum_{i=0}^{\infty} E^{\frac{i}{2}}\zeta_i$	p.14
ζ_T	Vorticity of the lid, $\zeta_T = 2\frac{\epsilon}{\lvert\epsilon\rvert}$	p.15
θ	Azimuthal angle from "due east"	p.13
$\hat{\theta}$	Azimuthal unit vector	p.130
θ_j	Azimuthal coordinate of grid index j, $\theta_j = (j-1)\Delta_\theta$	p.131
Λ	Aspect ratio of the tank, $\Lambda = \frac{a}{H_o}$	p.13
ν	Dimensional kinematic viscosity of the fluid	p.13
σ	Correction to Ekman pumping due to bottom slope, $\sigma = \sqrt[4]{1+s^2}$	p.15
ϕ, ψ	Scalar potential and streamfunction for the horizontal velocity; $\mathbf{u}_H = \hat{\mathbf{k}} \times \nabla_H\psi + \nabla_H\phi$	Eq. (2.4), p.13
$\boldsymbol{\omega}$	Relative vorticity vector, $\boldsymbol{\omega} = \nabla \times \mathbf{u}$	p.14
Ω	Dimensional angular velocity of base	Fig. 2.1, p.11
∇_H	Horizontal gradient operator	p.13

Bibliography

Agra, C. & Nof, D. 1993 Collision and separation of boundary currents. *Deep-Sea Res. 1* **40**, 2259–2282.

Allen, J. S., Barth, J. A. & Newberger, P. A. 1990 On intermediate models for barotropic continental shelf and slope flow fields. Part I: Formulation and comparison of exact solutions. *J. Phys. Oceanogr.* **20**, 1017–1042.

Alligood, K. T., Sauer, T. D. & Yorke, J. A. 1997 *Chaos - an introduction to dynamical systems*, 1st edn. New York: Springer-Verlag.

Arakawa, A. 1966 Computational design for long-term numerical integration of the equations of fluid motion: Two-dimensional incompressible flow. Part 1. *J. Comput. Phys.* **1**, 119–143.

Baines, P. G. & Hughes, R. L. 1996 Western boundary current separation: Inferences from a laboratory model. *J. Phys. Oceanogr.* **26**, 2576–2588.

Baker, D. J. & Robinson, A. R. 1969 A laboratory model for the general ocean circulation. *Phil. Trans. Roy. Soc. Lond. A.* **265**, 533–566.

Batchelor, G. K. 1956 On steady laminar flow with closed streamlines at large Reynolds number. *J. Fluid Mech.* **1**, 177–190.

Beardsley, R. C. 1969 A laboratory model of the wind-driven ocean circulation. *J. Fluid Mech.* **38**, 255–271.

Beardsley, R. C. 1972 A numerical investigation of a laboratory analogy of the wind-driven ocean circulation. In *NAS Symposium on Numerical Models of Ocean Circulation*, p. 311. Durham, New Hampshire: National Academy of Sciences.

Beardsley, R. C. 1973 A numerical model of the wind-driven ocean circulation in a circular basin. *Geophys. Fluid Dyn.* **4**, 211–241.

Beardsley, R. C. 1975 The 'sliced-cylinder' laboratory model of the wind-driven ocean circulation. Part 2: Oscillatory forcing and Rossby wave resonance. *J. Fluid. Mech.* **69**, 41–64.

Beardsley, R. C. & Robbins, K. 1975 The 'sliced-cylinder' laboratory model of the wind-driven ocean circulation. Part 1: Steady forcing and topographic Rossby wave instability. *J. Fluid Mech.* **69**, 27–40.

Becker, A. & Page, M. A. 1990 Flow separation and unsteadiness in a rotating sliced cylinder. *Geophys. Astrophys. Fluid Dyn.* **55**, 89–115.

Becker, J. M. 1995 An inertial model of the general circulation in an ocean with bottom topography. In *'Aha Huliko' a Hawaiian winter workshop* (ed. D. Henderson & P. Mueller), pp. 125–130.

Becker, J. M. 1999 Effect of a western continental slope on the wind-driven circulation. *J. Phys. Oceanogr.* **29**, 512–518.

Becker, J. M. & Salmon, R. 1997 Eddy formation on a continental slope. *J. Mar. Res.* **55**, 181–200.

Bennetts, D. A. & Hocking, L. M. 1973 On nonlinear Ekman and Stewartson layers in a rotating fluid. *Proc. R. Soc. Lond. A.* **333**, 469–489.

Berloff, P. S. & McWilliams, J. C. 1999*a* Large-scale, low-frequency variability in wind-driven ocean gyres. *J. Phys. Oceanogr.* **29**, 1925–1949.

Berloff, P. S. & McWilliams, J. C. 1999*b* Quasigeostrophic dynamics of the western boundary current. *J. Phys. Oceanogr.* **29**, 2607–2634.

Berloff, P. S. & Meacham, S. P. 1997 The dynamics of an equivalent-barotropic model of the wind-driven circulation. *J. Mar. Res.* **55**, 407–451.

Berloff, P. S. & Meacham, S. P. 1998 On the stability of the wind-driven circulation. *J. Mar. Res.* **56**, 937–993.

Blandford, R. R. 1971 Boundary conditions in homogeneous ocean models. *Deep-Sea Res.* **18**, 739–751.

Böning, C. W. 1986 On the influence of frictional parameterization in wind-driven ocean circulation models. *Dyn. Atmos. Oceans* **10**, 63–92.

Briggs, W. L. 1980 A new class of steady solutions of the barotropic vorticity equation. *Dyn. Atmos. Oceans* **4**, 67–99.

Bryan, K. 1963 A numerical investigation of a nonlinear model of a wind-driven ocean. *J. Atmos. Sci.* **20**, 594–606.

Cessi, P. 1990 Recirculation and separation of boundary currents. *J. Mar. Res.* **48**, 1–35.

Cessi, P. 1991 Laminar separation of colliding western boundary currents. *J. Mar. Res.* **49**, 697–717.

Cessi, P., Condie, R. V. & Young, W. R. 1990 Dissipative dynamics of western boundary currents. *J. Mar. Res.* **48**, 677–700.

Cessi, P. & Ierley, G. R. 1993 Nonlinear disturbances of western boundary currents. *J. Phys. Oceanogr.* **23**, 1727–1735.

Cessi, P. & Ierley, G. R. 1995 Symmetry-breaking multiple equilibria in quasigeostrophic, wind-driven flows. *J. Phys. Oceanogr.* **25**, 1196–1205.

Cessi, P., Ierley, G. R. & Young, W. R. 1987 A model of the inertial recirculation driven by potential vorticity anomalies. *J. Phys. Oceanogr.* **17**, 1640–1652.

Chassignet, E. P. & Gent, P. R. 1991 The influence of boundary conditions on midlatitude jet separation in ocean numerical models. *J. Phys. Oceanogr.* **21**, 1290–1299.

Davey, M. K. 1978 Recycling flow over bottom topography in a rotating annulus. *J. Fluid Mech.* **87**, 497–520.

Dengg, J. 1993 The problem of Gulf Stream separation: A barotropic approach. *J. Phys. Oceanogr.* **23**, 2182–2200.

Dijkstra, H. A. & Katsman, C. A. 1997 Temporal variability of the wind-driven quasi-geostrophic double gyre ocean circulation: Basic bifurcation diagrams. *Geophys. Astrophys. Fluid Dyn.* **85**, 195–232.

Dijkstra, H. A. & Molemaker, M. J. 1999 Imperfections of the North Atlantic wind-driven ocean circulation: Continental geometry and windstress shape. *J. Mar. Res.* **57**, 1–28.

Douglas, Jr., J. 1955 On the numerical integration of $\partial^2 u/\partial x^2 + \partial^2 u/\partial y^2 = \partial u/\partial t$ by implicit methods. *J. Society of Industrial Applied Mathematics* **3**, 42–65.

Fofonoff, N. P. 1954 Steady flow in a frictionless homogeneous ocean. *J. Mar. Res.* **13**, 254–262.

Fofonoff, N. P. 1962 Dynamics of ocean currents. In *The Sea* (ed. M. N. Hill), pp. 323–395. New York/London: Interscience.

Frankignoul, C. & Müller, P. 1979 Quasi-geostrophic response of an infinite β-plane ocean to stochastic forcing by the atmosphere. *J. Phys. Oceanogr.* **9**, 104–127.

Friedlander, S. 1980 *An introduction to the mathematical theory of geophysical fluid dynamics*. North-Holland.

Greenspan, H. 1962 A criterion for the existence of inertial boundary layers in oceanic circulation. *Proc. Natl. Acad. Sci.* **48**, 2034–2039.

Greenspan, H. P. 1963 A note concerning topography and inertial currents. *J. Mar. Res.* **21**, 147–154.

Greenspan, H. P. 1968 *The theory of rotating fluids*, 1st edn. Cambridge: Cambridge University Press.

Greenspan, H. P. 1969 A note on the laboratory simulation of planetary flows. *Studies in Appl. Math.* **48**, 147–152.

Griffa, A. & Castellari, S. 1991 Nonlinear general circulation of an ocean model driven by wind with a stochastic component. *J. Mar. Res.* **49**, 53–73.

Griffa, A. & Salmon, R. 1989 Wind-driven ocean circulation and equilibrium statistical mechanics. *J. Mar. Res.* **47**, 457–492.

Griffiths, R. W. 1995 Flow regimes in the sliced-cylinder model of ocean circulation. In *12th Australasian Fluid Mechanics Conference* (ed. R. W. Bilger), pp. 275–278. Sydney, Australia: University of Sydney.

Griffiths, R. W. & Cornillon, P. 1994 Laboratory experiments with mid-latitude circulation in a two-layer ocean. In *4th International Symposium on Stratified Flows* (ed. E. J. Hopfinger). Grenoble, France.

Griffiths, R. W. & Kiss, A. E. 1999 Flow regimes in a wide 'sliced-cylinder' model of homogeneous β-plane circulation. *J. Fluid Mech.* **399**, 205–236.

Griffiths, R. W. & Veronis, G. 1997 A laboratory study of the effects of a sloping side boundary on wind-driven circulation in a homogeneous ocean model. *J. Mar. Res.* **55**, 1103–1126.

Griffiths, R. W. & Veronis, G. 1998 Linear theory of the effect of a sloping boundary on circulation in a homogeneous laboratory model. *J. Mar. Res.* **56**, 75–86.

Haidvogel, D., McWilliams, J. & Gent, P. 1992 Boundary current separation in a quasigeostrophic, eddy-resolving ocean circulation model. *J. Phys. Oceanogr.* **22**, 882–902.

Harrison, D. E. 1989 On climatological monthly mean wind stress and wind stress curl fields over the world ocean. *J. Clim.* **2**, 57–70.

Harrison, D. E. & Stalos, S. 1982 On the wind-driven ocean circulation. *J. Mar. Res.* **40**, 773–791.

Helfrich, K. R., Pedlosky, J. & Carter, E. 1999 The shadowed island. *J. Phys. Oceanogr.* **29**, 2559–2577.

Hellerman, S. & Rosenstein, M. 1983 Normal monthly wind stress over the world ocean with error estimates. *J. Phys. Oceanogr.* **13**, 1093–1104.

Holland, W. R. 1967 On the wind-driven circulation in an ocean with bottom topography. *Tellus* **19**, 582–600.

Holland, W. R. & Lin, L. B. 1975 On the generation of mesoscale eddies and their contribution to the oceanic general circulation. II: A parameter study. *J. Phys. Oceanogr.* **5**, 658–669.

Ierley, G. R. 1987 On the onset of inertial recirculation in barotropic general circulation models. *J. Phys. Oceanogr.* **17**, 2366–2374.

Ierley, G. R. & Ruehr, O. G. 1986 Analytic and numerical solutions of a nonlinear boundary-layer problem. *Studies in Appl. Math.* **75**, 1–36.

Ierley, G. R. & Sheremet, V. A. 1995 Multiple solutions and advection-dominated flows in the wind-driven circulation. Part 1: Slip. *J. Mar. Res.* **53**, 703–737.

Ierley, G. R. & Young, W. R. 1988 Inertial recirculation in a β-plane corner. *J. Phys. Oceanogr.* **18**, 683–689.

Ierley, G. R. & Young, W. R. 1991 Viscous instabilities in the western boundary layer. *J. Phys. Oceanogr.* **21**, 1323–1332.

Israeli, M. 1970 A fast implicit numerical method for time dependent viscous flows. *Studies in Appl. Math.* **49**, 327–349.

Jiang, S., Jin, F.-F. & Ghil, M. 1995 Multiple equilibria, periodic, and aperiodic solutions in a wind-driven, double-gyre, shallow-water model. *J. Phys. Oceanogr.* **25**, 764–786.

Kamenkovich, V. M., Sheremet, V. A., Pastushkov, A. R. & Belotserkovsky, S. O. 1995 Analysis of the barotropic model of the subtropical gyre in the ocean for finite Reynolds numbers. Part 1. *J. Mar. Res.* **53**, 959–994.

Kiss, A. E. 1999 Chaos in the 'sliced cone' model of wind-driven ocean circulation. Report on 1998 Summer Study Program in Geophysical Fluid Dynamics: Astrophysical and geophysical flows as dynamical systems. WHOI-99-01. Woods Hole Oceanographic Institution.

Kiss, A. E. 2000 Vorticity dynamics in the 'sliced cone' model of wind-driven circulation in a basin with continental shelves. *J. Mar. Res. (submitted)* .

Kiss, A. E. & Griffiths, R. W. 1998 Flow dynamics in the 'sliced cone' model of wind-driven ocean circulation. In *13th Australasian Fluid Mechanics Conference* (ed. M. C. Thompson & K. Hourigan), pp. 823–826. Melbourne, Australia: Monash University.

Krishnamurti, R. 1981 Laboratory modelling of the oceanic response to monsoonal winds. In *Monsoon Dynamics* (ed. J. Lighthill & R. P. Pearce), pp. 557–576. Cambridge University Press.

Krishnamurti, R. & Na, J. Y. 1978 Experiments in ocean circulation modelling. *Geophys. Astrophys. Fluid Dyn.* **11**, 13–21.

Kubokawa, A. & McWilliams, J. C. 1996 Topographic ocean gyres: A western boundary slope. *J. Phys. Oceanogr.* **26**, 1468–1479.

Le Provost, C. & Verron, J. 1987 Wind-driven ocean circulation transition to barotropic instability. *Dyn. Atmos. Oceans* **11**, 175–201.

Leonard, B. P. 1984 Third-order upwinding as a rational basis for computational fluid dynamics. In *Computational techniques and applications: CTAC-83* (ed. J. Noye & C. Fletcher). Elsevier.

Levitus, S. 1982 Climatological atlas of the world ocean. Professional paper 13. NOAA.

Matsuura, T. & Yamagata, T. 1986 A numerical study of a viscous flow past a right circular cylinder on a β-plane. *Geophys. Astrophys. Fluid Dyn.* **37**, 129–164.

McWilliams, J. C. 1996 Modeling the oceanic general circulation. *Ann. Rev. Fluid Mech.* **28**, 215–248.

McWilliams, J. C. & Gent, P. R. 1980 Intermediate models of planetary circulations in the atmosphere and ocean. *J. Atmos. Sci.* **37**, 1657–1678.

Meacham, S. P. & Berloff, P. S. 1997*a* Barotropic, wind-driven circulation in a small basin. *J. Mar. Res.* **55**, 523–563.

Meacham, S. P. & Berloff, P. S. 1997*b* Instabilities of a steady, barotropic, wind-driven circulation. *J. Mar. Res.* **55**, 885–913.

Merkine, L.-O., Mo, K. C. & Kalnay, E. 1985 On Fofonoff's mode. *Geophys. Astrophys. Fluid Dyn.* **32**, 175–196.

Moore, D. W. 1963 Rossby waves in ocean circulation. *Deep-Sea Res.* **10**, 735–748.

Moro, B. 1988 On the nonlinear Munk model, I: Steady flows. *Dyn. Atmos. Oceans* **12**, 259–287.

Moro, B. 1990 On the nonlinear Munk model, II: Stability. *Dyn. Atmos. Oceans* **14**, 203–227.

Munk, W. H. 1950 On the wind-driven ocean circulation. *J. Meteorology* **7**, 79–93.

Niiler, P. P. 1966 On the theory of wind-driven ocean circulation. *Deep-Sea Res.* **13**, 597–606.

Oguz, T., Aubrey, D. G., Latun, V. S., Demirov, E., Koveshnikov, L., Sur, H. I., Diaconu, V., Besiktepe, S., Duman, M., Limeburner, R. & Eremeev, V. 1994 Mesoscale circulation and thermohaline structure of the Black Sea observed during Hydroblack '91. *Deep-Sea Res., Part I* **41**, 603–628.

Oguz, T. & Malanotte-Rizzoli, P. 1996 Seasonal variability of wind and thermohaline-driven circulation in the Black Sea - modeling studies. *J. Geophys. Res. Oceans* **101**, 16551–16569.

Özgökmen, T. M., Chassignet, E. P. & Paiva, A. M. 1997 Impact of wind forcing, bottom topography, and inertia on midlatitude jet separation in a quasigeostrophic model. *J. Phys. Oceanogr.* **27**, 2460–2476.

Page, M. A. 1981 Rotating fluids at low Rossby number. PhD thesis, University College, London.

Page, M. A. 1982 A numerical study of detached shear layers in a rotating sliced cylinder. *Geophys. Astrophys. Fluid Dyn.* **22**, 51–69.

Parsons, A. T. 1969 A two-layer model of Gulf Stream separation. *J. Fluid Mech.* **39**, 511–528.

Peaceman, D. W. & Rachford, Jr., H. H. 1955 The numerical solution of parabolic and elliptic differential equations. *J. Society of Industrial Applied Mathematics* **3**, 28–41.

Pearson, C. E. 1965 A computational method for viscous flow problems. *J. Fluid Mech.* **21**, 611–622.

Pedlosky, J. 1965*a* A necessary condition for the existence of an inertial boundary layer in a baroclinic ocean. *J. Mar. Res.* **23**, 69–72.

Pedlosky, J. 1965*b* A study of the time dependent ocean circulation. *J. Atmos. Sci.* **22**, 267–272.

Pedlosky, J. 1971 Geophysical fluid dynamics. In *Mathematical problems in the geophysical sciences* (ed. W. H. Reid), pp. 1–60. American Mathematical Society.

Pedlosky, J. 1987*a* *Geophysical Fluid Dynamics*, 2nd edn. New York: Springer.

Pedlosky, J. 1987*b* On Parsons' model of the ocean circulation. *J. Phys. Oceanogr.* **17**, 1571–1582.

Pedlosky, J. 1996 *Ocean Circulation Theory*, 1st edn. Berlin: Springer.

Pedlosky, J. & Greenspan, H. P. 1967 A simple laboratory model for the oceanic circulation. *J. Fluid Mech.* **27**, 291–304.

Pedlosky, J., Pratt, L. J., Spall, M. A. & Helfrich, K. R. 1997 Circulation around islands and ridges. *J. Mar. Res.* **55**, 1199–1251.

Peixoto, J. P. & Oort, A. H. 1992 *Physics of climate*, 1st edn. New York: American Institute of Physics.

Plaut, G., Ghil, M. & Vautard, R. 1995 Interannual and interdecadal variability in 335 years of Central England temperatures. *Science* **268**, 710–713.

Press, W. H., Teukolsky, S. A., Vetterling, W. T. & Flannery, B. P. 1992 *Numerical recipes in FORTRAN: The art of scientific computing*, 2nd edn. Cambridge: Cambridge University Press.

Rhines, P. B. 1986 Vorticity dynamics of the oceanic general circulation. *Ann. Rev. Fluid Mech.* **18**, 433–497.

Rhines, P. B. & Young, W. R. 1982*a* Homogenization of potential vorticity in planetary gyres. *J. Fluid Mech.* **122**, 347–367.

Rhines, P. B. & Young, W. R. 1982*b* A theory of the wind-driven circulation. I: Mid-ocean gyres. *J. Mar. Res.* **40**, 559–596.

Roache, P. J. 1982 *Computational fluid dynamics*, 2nd edn. Albuquerque: Hermosa.

Salmon, R. 1992 A two-layer Gulf Stream over a continental slope. *J. Mar. Res.* **50**, 341–365.

Salmon, R. 1998 Linear circulation theory with realistic bathymetry. *J. Mar. Res.* **56**, 833–884.

Schlichting, H. 1968 *Boundary-layer theory*, 6th edn. New York: McGraw-Hill.

von Schwind, J. J. 1980 *Geophysical fluid dynamics for oceanographers*, 1st edn. Englewood Cliffs, New Jersey: Prentice-Hall.

Sheremet, V. A., Ierley, G. R. & Kamenkovich, V. M. 1997 Eigenanalysis of the two-dimensional wind-driven ocean circulation problem. *J. Mar. Res.* **55**, 57–92.

Sheremet, V. A., Kamenkovich, V. M. & Pastushkov, A. R. 1995 Analysis of the barotropic model of the subtropical gyre in the ocean for finite Reynolds numbers. Part 2. *J. Mar. Res.* **53**, 995–1024.

Speich, S., Dijkstra, H. A. & Ghil, M. 1995 Successive bifurcations in a shallow-water model applied to the wind-driven ocean circulation. *Nonlin. Process. Geophys.* **2**, 241–268.

Spitz, Y. H. & Nof, D. 1991 Separation of boundary currents due to bottom topography. *Deep-Sea Res.* **38**, 1–20.

STEWARTSON, K. 1957 On almost rigid rotations. *J. Fluid Mech.* **3**, 17–26.

STOMMEL, H. 1948 The westward intensification of wind-driven ocean currents. *Trans. Am. Geophys. Union* **29**, 202–206.

SVERDRUP, H. 1947 Wind-driven currents in a baroclinic ocean: with application to the equatorial currents of the eastern Pacific. *Proc. Natl. Acad. Sci. USA* **33**, 318–326.

TRENBERTH, K. E., LARGE, W. G. & OLSON, J. G. 1990 The mean annual cycle in global ocean wind stress. *J. Phys. Oceanogr.* **20**, 1742–1760.

VERONIS, G. 1966*a* Generation of mean ocean circulation by fluctuating winds. *Tellus* **18**, 67–76.

VERONIS, G. 1966*b* Wind-driven circulation. Part 2: Numerical solutions of the non-linear problem. *Deep-Sea Res.* **13**, 31–55.

VERONIS, G. 1970 Effect of fluctuating winds on ocean circulation. *Deep-Sea Res.* **17**, 421–434.

VERONIS, G. 1973*a* Large scale ocean circulation. *Adv. Appl. Mech.* **13**, 1–92.

VERONIS, G. 1973*b* Model of world ocean circulation: I. Wind-driven, two layer. *J. Mar. Res.* **31**, 228–288.

VERRON, J. & BLAYO, E. 1996 The no-slip condition and separation of western boundary currents. *J. Phys. Oceanogr.* **26**, 1938–1951.

VERRON, J. & JO, J.-H. 1994 On the stability of wind-driven barotropic ocean circulations. *Fluid Dyn. Res.* **14**, 7–27.

VERRON, J. & LE PROVOST, C. 1991 Response of eddy-resolved general circulation numerical models to asymmetrical wind forcing. *Dyn. Atmos. Oceans* **15**, 505–533.

WELANDER, P. 1968 Wind-driven circulation in one- and two-layer oceans of variable depth. *Tellus* **20**, 1–15.

WILLEBRAND, J. 1978 Temporal and spatial scales of the wind field over the North Pacific and North Atlantic. *J. Phys. Oceanogr.* **8**, 1080–1094.